Reactive jet impingement bioprinting of high cell density gels for bone microtissue fabrication

Ricardo da Conceicao Ribeiro[1], Deepali Pal[2], Ana Marina Ferreira[1], Piergiorgio Gentile[1], Matthew Benning[1], Kenneth Dalgarno[1,3]

[1] School of Engineering, Newcastle University, UK;

[2] Wolfson Childhood Cancer Research Centre, Northern Institute for Cancer Research, Newcastle University, UK;

[3] Author to whom any correspondence should be addressed.

Abstract

Advances in three-dimensional (3D) cell cultures offer new opportunities in biomedical research and drug development. However, there are still challenges to overcome, including the lack of reliability, repeatability and complexity of tissues obtained by these techniques. In this study, we describe a new bioprinting system called Reactive Jet Impingement (ReJI) for the bioprinting of cell-laden hydrogels. Droplets of gel precursor solutions are jetted at one another such that they meet and react in mid-air before the gel droplets fall to the substrate. This technique offers a combination of deposition rate, cell density and cell viability which is not currently matched by any other bioprinting technique. The importance of cell density is demonstrated in the development of bone microtissues derived from immortalized human bone marrow stem cells. The cells were printed with high viability within a collagen-alginate-fibrin gel, and tissue specific gene expression shows significantly higher tissue maturation rates using the ability of the ReJI system to deposit gels with a high cell density.

1. Introduction

In vitro assays must effectively recapitulate the human environment in order to provide value in the understanding of biological processes. However, many *in vitro* models remain two-dimensional, despite 2D models being unable to simulate the human environment [1, 2]. Gene expression, metabolic activity, cell physiology and morphology and spatial organization are all affected by cells being in 2D rather than 3D, and the use of 2D cultures has been cited as one reason for the large attrition rate in drug trials [3, 4].

Three-dimensional cell culture techniques allow the reproduction of the cell physiological environment [1-4]. Spheroids, organoids, organs-on-chips or scaffold-based cell cultures [5-10] constitute some of the novel 3D systems that can emulate natural cell-cell interactions. Scaling-up the rate of production of these structures could offer improved *in vitro* drug assays that would grant an increase in reliability and repeatability of pre-clinical screening. Additionally, the ability to mimic the human microenvironment could allow a decrease in animal testing, whilst at the same time lowering cost and accelerating the process. However, each 3D cell culture system carries its own advantages and disadvantages, but generally present problems over reliability and repeatability, but also in terms of tissue complexity [11-14].

Furthermore, advances in tissue engineering, biomaterials and additive manufacturing have enabled rapid development of bio-inspired three-dimensional structures. Microtissues or organ-like structures, such as mini-livers [15, 16], urethras [17] or muscles [18], have recently been developed by different bioprinting techniques. Currently, to obtain 3D structures, the most used bioprinting techniques are drop-on-demand (DoD) printing (inkjet and microvalve printing) and microextrusion bioprinting. The first relies in a system that through the activation of a piezoelectric crystals, heating nozzle or mechanical valves, to produce droplets with volumes ranging from pL to µL [19]. On the other hand, microextrusion printing uses pneumatic or mechanical systems to extrude continuous filaments of material [19, 20]. DoD printing techniques allow printing with high level of accuracy and speed, depositing hundreds to thousands of pL to nL droplets per second. However, inkjets commonly suffer nozzle blockage due to cell aggregation and, therefore, high cell densities are not generally possible. Both inkjet and microvalve methods are restricted to low viscosity materials (3-30 mPa/s) with a crosslinking step necessary to produce solid 3D structures. On the other hand, microextrusion bioprinting allows the printing of physiological cell densities, but it is a slow process and cells suffer high shear stress, resulting in increased cell death [19,20].

High cell density encapsulation is essential to develop tissue like cell-cell interactions [21]. However, obtaining physiological cell densities remains one of the biggest issues to achieve microtissues through bioprinting. One of the most famous concepts to develop tissue-like structures is “tissue spheroids as building blocks”, where hundreds of spheroids, carrying thousands of cells are disposed in a certain shape to fuse together forming a tissue [22]. This allows macroscopic specimens, such as cardiac patches [23], vascular or nerve grafts, to be produced [24]. However, spheroids present several downsides, such as long-term cell culture problems and repeatability issues [25,26]. Advances in extrusion bioprinters and in-house techniques have allowed higher cell densities, obtaining cartilaginous tissue by using $20x10^6$ cells/mL nanocellulose bio-inks

[27] or by adopting $40x10^6$ cells/mL multi-material bio-inks [18]. On the other hand, bone constructs were developed from $8x10^6$ cells/mL gel-loaded microcarriers bio-inks [28]. However, the number of reported studies with high cell densities is still scarce due the difficulty inherent in the bioprinting of these bio-inks.

Here, we report for the first time a new printing system entitled Reactive Jet Impingement (ReJI), that combines the speed and accuracy of the DoD printing with the ability of depositing physiological cell densities. We show the functionality of our bioprinting technique by printing highly viable cell-laden collagen/alginate/fibrin hydrogels that allow long-term cell culture. We also show that, when human mesenchymal stromal cells (MSCs) are printed at high densities, they rapidly differentiate towards bone and produce highly organized tissue structures with mineralisation and tissue-specific gene expression in less than 14 days.

2. Materials and methods

2.1. Reagents

Unless otherwise stated, reagents were obtained from Sigma-Aldrich, Gillingham, UK.

2.2. Cell Culture

Immortalized human bone marrow stem cells using human telomerase reverse transcriptase (BMSC-hTERT) (kindly donated by Professor Paul Genever, York University [29]), were grown in high-glucose with pyruvate Dulbecco's Modified Eagle's Medium (DMEM; Life Technologies, Carlsbad, USA) supplemented with 10% fetal bovine serum (FBS; Thermo Fisher Scientific, Loughborough, UK) and 5000 U/mL penicillin/streptomycin at 37 °C and 5% CO_2. For osteogenic medium, the same DMEM preparation was supplemented with L-Ascorbic acid 2-phosphate sesquimagnesium salt, ß-Glycerophosphate, and Dexamethasone, at a final concentration of 50 µg/mL, 5 mM, and 10 nM, respectively. Medium was changed every 3 days during incubation periods.

2.3. Preparation of gel precursors

CAF hydrogels were optimised from the original research reported by Montalbano *et al* [30]. Prior to the pre-gel solution preparation, a 37.5 mg/mL fibrinogen (from bovine plasma - Type I-S, 65-85% protein (⩾75% of protein is clottable)) solution was obtained by gently dissolving fibrinogen in Dulbecco's Phosphate Buffered Saline (DPBS) without calcium and magnesium at 37 °C. A 25 mg/mL NaAlg in DPBS without calcium and magnesium solution was also formulated. To achieve the pre-gel solution, the fibrinogen and NaAlg solutions were slowly mixed, followed by carefully mixing of the prior preparation with 6 mg/mL pepsin soluble collagen solution in HCl (Collagen Solutions, Glasgow, UK) to a ratio of 1:2:8 of collagen, alginate and fibrinogen (CAF), respectively. As crosslinking solution, a 500 U/mL of thrombin (40-300 NIH units/mg protein) dissolved in high-glucose with pyruvate DMEM with 0.1% of $CaCl_2$ was used.

2.4. Printing apparatus

A Jetlab 4 (Microfab Technologies, Inc., Plano, USA) was adapted to our in-house printhead (ReJI) [31]. The ReJI system was composed by two solenoid valves INKX0514950A – microvalves – (The Lee Company, Westbrook Center, USA) located in opposite sides at 55º of inclination, connected to two spike and hold drivers (The Lee Company) to control the open and closure of the valves. The microvalves were also connected to the ink loading reservoirs, which are attached to the pneumatics controller CT-PT4 (Microfab Technologies, Inc.). Droplet ejection was obtained by applying an

electrical impulse in the form of a rectangular waveform with a dwell time, amplitude and frequency of 800 µs, 5 V and 400 Hz.

2.5. Compression and degradation tests

Compression tests were performed using a tensile tester EZ-SX (Shimadzu, Kyoto, Japan) equipped with a 20 N load cell. Samples were cut to a parallelepiped-like shape with a dimension average of 6.5x6.5x3.3 mm. The crosshead speed was set at 1 $mm \cdot min^{-1}$ and the tests were carried at room temperature. Compressive modulus was calculated on the linear elastic regime (in the range 10-20%). Then, CAF hydrogel degradation was obtained through gravimetric analysis. Once printed, each sample was wiped with filter paper and weighted (W_i) before immersion in high-glucose with pyruvate DMEM at 37 ºC and 5% CO_2 for 1, 3, 7, and 14 days. After the test end, samples were dried with filter paper to remove the excess of medium and reweighted (W_f). The degradation was calculated using the equation 1:

$$Degradation\ (\%) = 1 - \frac{W_f}{W_i} \times 100 \qquad \text{Equation 1}$$

2.6. Glucose uptake

A 0.06845 mg/mL 2-(N-(7-Nitrobenz-2-oxa-1,3-diazol-4-yl)Amino)-2-Deoxyglucose (2-NBDG; Thermo Fisher Scientific) in PBS was prepared and protected from light. After washing the samples with PBS, 2 mL 2-NBDG solution was added to each gel during different time-points. Once reached the time-point, gels were transferred to a new well-plate with PBS to release the absorbed 2-NBDG. The resultant was read at an excitation/emission of 465/540 nm using a LS-50B Luminescence Spectrometer (Perkin Elmer, Waltham, USA).

2.7. Cell-loaded CAF gels printing

To obtain cell suspensions with $4x10^6$ cells/mL and $40x10^6$ cells/mL, after a DPBS wash, MSCs were detached with 0.25% trypsin solution, centrifuged at 1200 rpm for 5 min and counted. The desired cell suspension was obtained by mixing 1 mL of 500 U/mL of thrombin solution with 0.1% of $CaCl_2$ with the cell pellet. The pre-gel CAF and cell-containing crosslinking solution were loaded at 37 ºC into two reservoirs and the cell-filled hydrogels were fabricated by simultaneous droplet jetting from each precursor that, when mixed in air, formed a gel before reaching the stage. To jet the pre-gel and cell-containing crosslinking solution, the pressure system was in the range of 270–310 mmHg and 450–550 mmHg, respectively. A specific pattern was achieved by coding and loading a script into the Jetlab4 software – each 10x8 pixels and 16-layer structure was obtained in 4 min. After printing, the cell-laden construct was incubated in osteogenic medium at 37 °C and 5% CO_2.

2.8. Fluorophore staining for confocal microscopy

Cell-loaded gels were fixed immediately after printing, 7 or 14 days of incubation using pre-warmed 4% paraformaldehyde solution for 25 min at room temperature. Cells were washed three times using 0.1% DPBS/Tween 20 and phalloidin (1 mg/mL in methanol) added during a 40-min light-protected incubation period at room temperature. After further washing with 0.1% DPBS/Tween 20, 4,6-diamidino-2-phenylindole (DAPI; 1:2500 solution, Vector Laboratories, Burlingame, USA) was added, and the solution was subjected to a 25-min light-protected incubation period at room temperature. Cells were washed and resuspended in 0.1% DPBS/Tween 20. Fixed samples were stored protected from light at 4 °C until visualized using a Nikon A1R (Nikon, Minato, Japan) at 10× magnification.

2.9. Morphology study by scanning electron microscopy

The cell morphology in the hydrogels was examined using a Tescan Vega LMU (Tescan, Cambridge, UK). Samples were fixed using a pre-warmed solution of 2% glutaraldehyde (TAAB Laboratory Equipment, Reading, UK) in Sorensons buffer. The samples were then stored at 4 °C overnight followed by dehydration steps using 25%, 50%, 75%, and 100% ethanol. Samples were stored at 4 °C in 100% ethanol until critical point dried using a BAL-TEC 030 Critical Point Dryer (Leica Geosystems Ltd, Milton Keynes, UK). Finally, gels were mounted on carbon discs (TAAB Laboratory Equipment) and gold-coated using a Polaron E5000 SEM Coating unit (Quorum Technologies Ltd (Polaron Division), East Sussex, UK).

2.10. Cell viability, proliferation, and ALP assays

The Live/Dead (Molecular Probes by Life Technologies, Carlsbad, USA) assay was used to evaluate the cell viability at different time-points. Reagent stock solutions were removed from the freezer and warmed to room temperature and were prepared using the manufacturer's recommendations to obtain a 4 µM ethidium homodimer (EthD-1) and 2 µM calcein AM solution. After 1h incubation at room temperature, samples were visualized using a Nikon A1R confocal microscope at 10× magnification. Cell proliferation was assessed at day 0, 7 and 14 using PicoGreen DNA quantitation assay (Thermo Fisher Scientific). Standards were prepared following manufacturer's recommendations. After a certain time-point, samples were stored frozen (-20 ºC) in 1.5 mL of sterile molecular biology reagent grade water. Before analysis, samples undergone three cycles of freezing and thawing, following 20 minutes on an ultrasonication bath to release all the DNA. 50 µL of the cell lysate were combined with 100 µL 1xTE and 150 µL PicoGreen dye buffer (1:200) before loading a 96 opaque well plate in triplicates. After a 10-min room temperature incubation protected from light, samples were read (excitation/emission 485/530 nm) using a Spectramax Gemini XPS microplate reader (Molecular Devices, San José, USA). The ALP activity was measured using the same cell

lysate combined with 1-Step PNPP Substrate Solution (Thermo Fisher Scientific). The results were compared with the dilution of a p-nitrophenol standard solution. For each sample, in triplicate and in a transparent 96-well plate, 80 μL of the cell lysate was combined with 120 μL of 1-Step PNPP Substrate Solution. After a 1-hour incubation at 37 °C, the absorbance was read at 405 nm using a Biotek ELX800 (Biotek, Winooski, USA).

2.11. Gene expression analysis through RT–PCR array

RNA of cells was extracted after specific time-points using RNeasy Mini Kit (Qiagen, Hilden, Germany) following manufacturer's recommendations. The extracted RNA concentration was measured using a Nanodrop (ND-1000, NanoDrop Technologies, USA). cDNA synthesis was performed using RT2 First Strand Kit (Qiagen), following manufacturer's protocol. Before loading the RT-PCR Array for Human Osteogenesis (Qiagen), SYBR-green (Qiagen) was added to the synthetized cDNA. Gene expression was analysed using a ViiA7 384-well block (Applied Biosystems, Foster City, USA).

2.12. Statistical analysis

Data are expressed as mean ± standard deviation. Mean values and standard deviations were calculated from three independent experiments of triplicates per group. Comparisons were performed by one-way analysis of variance (ANOVA) in conjunction with Tukey's multiple comparison test using levels of statistical significance of $P < 0.05$ (*), $P < 0.01$ (**), $P < 0.001$ (***), and $P < 0.0001$ (****).

3. Results

3.1. Reactive jet impingement characterisation

The concept behind the ReJI system (figure 1) relies on two microvalves connected to different cartridges and directed to jet droplets so that drops can meet in mid-air and form a gel before reaching the stage (figure 1(b)). Each microvalve is attached to a spike and hold driver that is responsible for the opening and closing of the microvalve, but also connected to the pneumatics system and to the printer input that controls the electrical waveform. Through optimization of all these parameters, which are dependent on the material to be jetted, it is possible to achieve simultaneous droplet jetting (figure 2(a)). The system is enclosed inside an environmental chamber.

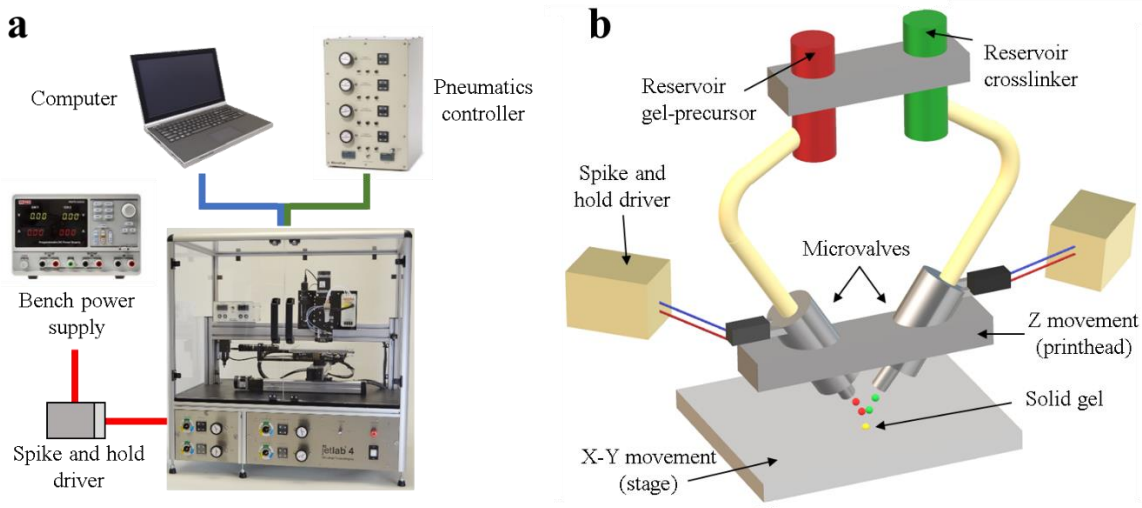

Figure 1. Reactive Jet Impingement system. (a) Overview of the main components: Computer, pneumatics controller, bench power supply connected to a spike and hold driver and a jetlab4 printer. (b) Illustration of the ReJI printhead, which is composed by two microvalves, located in opposite sides, connected to a spike and hold driver, for electrical input controlling, and to the ink reservoirs. The solid gel (yellow) is formed upon mixing in mid-air between the gel-precursor (green) and crosslinking (red) droplets.

The printing technique is reliable, printing gel droplets of similar sizes and at equidistant locations, over multiple layers (figure 2(b) and (c)). The optimised printing parameters for the collagen-alginate-fibrin gel used in this study are listed in figure 2(d), with collagen, alginate and fibrin deposited through one microvalve, and the thrombin and $CaCl_2$ deposited through the other. Due to the non-cytotoxic effect of thrombin solutions [32] and low viscosity when compared to the gel-precursor, cells were loaded into the crosslinking solution.

3.2. CAF hydrogel properties

CAF hydrogels were optimised from the original research reported by Montalbano *et al* [30] and produced with nominal dimensions of 11 x 8 x 3 mm. Our first analysis tested the ability of acellular printed CAF hydrogels with properties suitable for cell maintenance during long cell culture periods. The hydrogel contains natural materials, including proteins, and it was necessary to guarantee that no medium component would affect the printed hydrogel for long time-intervals. It was established that printed structures showed comparable levels of degradation at different time-points, losing around 30% of its total mass after any incubation time-point inspected (figure 3(a)). To support cells inside the hydrogels, it is crucial that molecules are be able to be delivered to the most inner site of it. Therefore, the CAF hydrogel absorbance and molecule permeation capabilities has been studied using a 2-(N-(7-Nitrobenz-2-oxa-1,3-diazol-4-yl)Amino)-2-Deoxyglucose (2-NBDG) solution, a fluorescent glucose analogue (figure 3(b)). Rapid 2-NBDG uptake in the first 30 min was observed, reaching a close-to-maximum uptake plateau between 30 and 60 min (figure 3(b)) for 3 mm thick specimens. The mechanical properties in compression of printed CAF gels gave a compressive

modulus of 1120±40 Pa calculated from the linear region of the stress-strain curve, in the 10-20% strain interval (figure 3(c)). The hydrogel microstructure was observed by scanning electron microscopy (SEM; figure 2(d)). A highly porous system was revealed by SEM images of samples at different time-points. It was observed that incubation in cell medium at 37°C and 5% CO_2 for 14 days did not change the hydrogel structure, presenting a similar morphology to the freshly printed samples. Outer and inner porosity can be seen with more detail in supplementary figure 1.

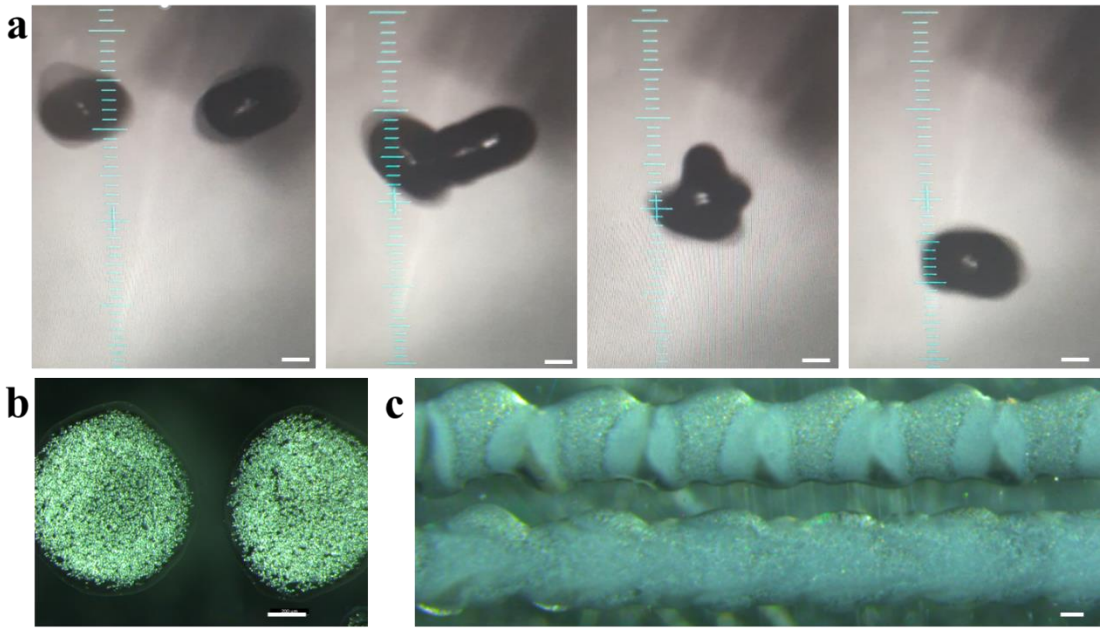

d

Material	[C] (mg/mL)	Frequency (Hz)	Pressure (mmHg)	Dwell Time (µs)
CAF	Col – 0.54 NaAlg – 4.54 Fib – 27.27	400	450	800
500 U/mL Thrombin with $CaCl_2$	$CaCl_2$ – 1.00	400	290	800
500 U/mL Thrombin with $CaCl_2$ Loaded with $4x10^6$ cells/mL	$CaCl_2$ – 1.00	400	290	800
500 U/mL Thrombin with $CaCl_2$ Loaded with $40x10^6$ cells/mL	$CaCl_2$ – 1.00	400	300	800

Figure 2. ReJI printing technique. (a) Stroboscopic images of gel-precursor and crosslinking droplets meeting in air. CAF gel loaded with 40 x 10^6 cells: (b) printed in single layer droplets 0.795±0.083 mm dia; and (c) after 2 (top) and 5 (bottom) layers, respectively. (d) Optimised parameters used to print hydrogel precursors using ReJI printhead. Scale bars represent 200 µm.

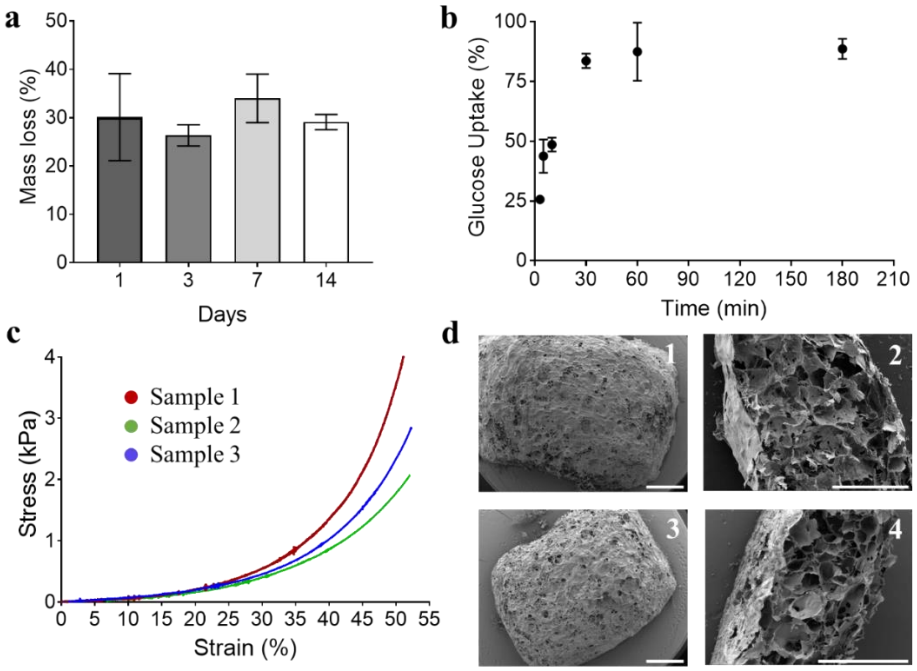

Figure 3. CAF gel properties. (a) CAF gel mass loss after incubation in medium during 1 to 14 days. Gels did not degrade, losing a maximum of 40% of its weight during the studied time-points. (b) CAF gel glucose uptake. A plateau on the uptake of 2-NBDG was reached 30 to 60 minutes (corresponding to 85-90% of maximum uptake) after putting the gel in contact with this solution. (c) Uniaxial compression of CAF gels. A compression modulus of (1.125±0,042) kPa was obtained for 10-20% strain interval. (d) CAF gel morphology after freeze drying. The SEM images show a highly porous fibre-like structure. 1 and 2 show a gel fixed immediately after printing and 3 and 4 reveal a gel fixed after 14 days of incubation in medium. Scale bars represent 1 mm. Each assay was conducted in triplicate.

3.3. Printing of cell-loaded CAF hydrogels

The ReJI printhead allowed for the rapid creation of high cell density droplet-on-demand printed hydrogels, with two concentrations of MSCs used: 4 and 40 million cells per mL. The printed hydrogels, independent of the cell number, presented identical structures with dimensions 11 x 8 x 3 mm after printing, however, the hydrogel was more opaque with the increased cell density (figure 4(a)). The cell distribution after printing was observed through confocal microscopy (figure 4(b)). An increment on the cell number per unit of area was naturally noticed, showing higher cell dispersion on $4x10^6$ cells/mL hydrogels and super-confluent hydrogels when using $40x10^6$ cells/mL inks. The encapsulated MSCs in CAF hydrogels had their viability evaluated by Live/Dead assay instantly after printing (supplementary figure 2) and after 7 and 14 days (figure 4(c) of incubation in osteogenic medium. Both cell densities presented almost no cell death after printing, with cytocompatibility maintained 7 and 14 days later.

A PicoGreen assay was used to examine cell proliferation in the hydrogels (figure 4(d)). As expected, $40x10^6$ cells/mL hydrogels presented an increased cell number on day 0, about $(5.22\pm1.30)x10^6$ cells per gel, when compared to the low-density structures, which had approximately 9-fold less cells, $(0.61\pm0.03)x10^6$. However, at day 7, a reduction in cell number in the high-density hydrogels and an increase in cell number in the low

density hydrogels, led to similar cell numbers across all the samples (approximately $2.7x10^6$ cells per gel). At day 14, although both hydrogel constructs had higher cell numbers, the $40x10^6$ cells/mL hydrogels presented the highest proliferation rate from day 7 to 14, increasing cell numbers to $(5.44\pm1.88)x10^6$ cells per gel. Using the PicoGreen kit standards, it was possible to calculate the DNA amount per cell – 5.6 pg/cell. Alkaline Phosphatase (ALP) was measured for each sample over the time course. The highest activity was observed at day 0, with no significant difference between the high and low cell density hydrogels. On days 7 and 14, the ALP value has decreased two to three-fold, with similar concentrations of PnPP per cell in both samples.

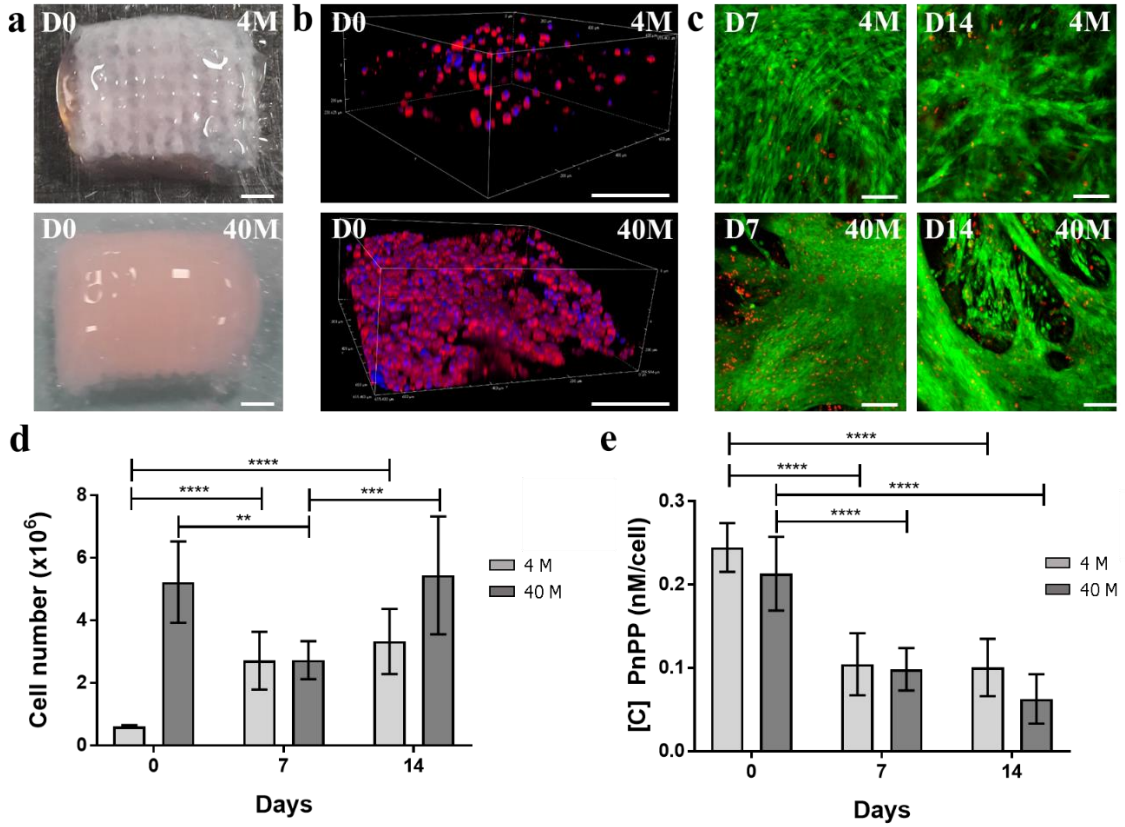

Figure 4. Cell number, viability and functionality. (a) Stereomicroscope pictures showing the morphology of the CAF gels loaded with $4x10^6$ cells/mL (top) and $40x10^6$ cells/mL (bottom) immediately after printing. Scale bar represents 2 mm. (b) Confocal microscopy volume stack showing cell distribution in CAF gels with different cell number. Scale bar represents 200 µm. (c) Live/Dead assay. Cell viability of MSCs after 7 and 14 days of incubation in osteogenic medium (live cells are represented in green and dead in red). Scale bar represents 100 µm. (d) Cell number (obtained by PicoGreen assay) present in CAF gels with $4x10^6$ and $40x10^6$ cells/mL after incubation during 0, 7 and 14 days in osteogenic medium. (e) PnPP concentration per cell obtained from ALP assay after incubation during 0, 7 and 14 days in osteogenic medium. *, **, ***, and **** indicate significant difference between groups at the levels $p < 0.05$, $p < 0.01$, $p < 0.001$, and $p < 0.0001$, respectively. Error bars represent the standard deviation (n = 3).

SEM and confocal microscopy were used to characterize the cell morphology and the degree of cell organization (figure 5). The images at day 0 (figure 5(a) and (b)) clearly illustrate the different cell densities. By day 14 the lower density gel structures change

from random cell alignment to a more organised morphology – cell alignment starts to be more apparent. In the high-density gels higher orientation and contact between cells is observable on day 7, and the degree of this organization clearly increases on day 14, with the development of clear tissue-like structures.

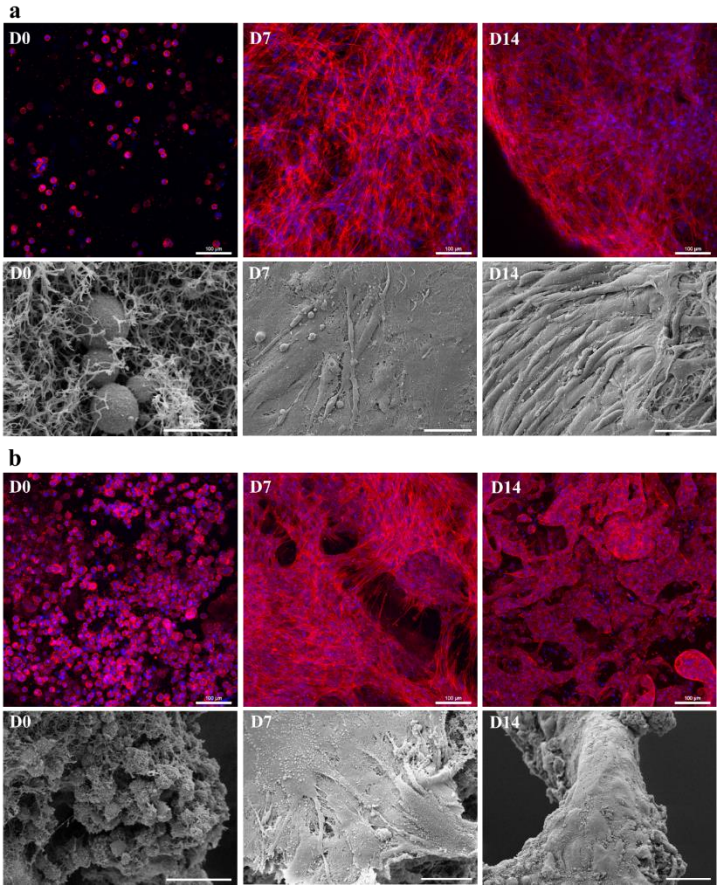

Figure 5. Cell and tissue morphology after incubation during 0, 7 and 14 days in osteogenic medium by confocal and scanning electron microscopy. (a) shows $4x10^6$ cells/mL loaded gels with an increase on cell organization along the incubation days (Red – F-Actin; Blue – Nucleus). Scale bars represent 100 µm for confocal images and 10, 20, and 50 µm, respectively, for SEM images. (b) For $40x10^6$ cells/mL loaded gels, cell density seems to favour cell migration, organisation and highly-defined tissue formation (Red – F-Actin; Blue – Nucleus). Scale bars represent 100 µm for confocal images and 50, 20, and 50 µm, respectively, for SEM images.

Increased calcium deposition was observed for the higher cell density samples (figure 6(a) and (b)), with differentiation affected by cell density, as cuboidal cells are already detected in the high-density hydrogels by day 7 (figure 6(c) and (d)). This is a clear sign of MSC differentiation into active osteoblasts. On the other hand, for the low-density hydrogels, cuboidal shaped cells are only observed at day 14.

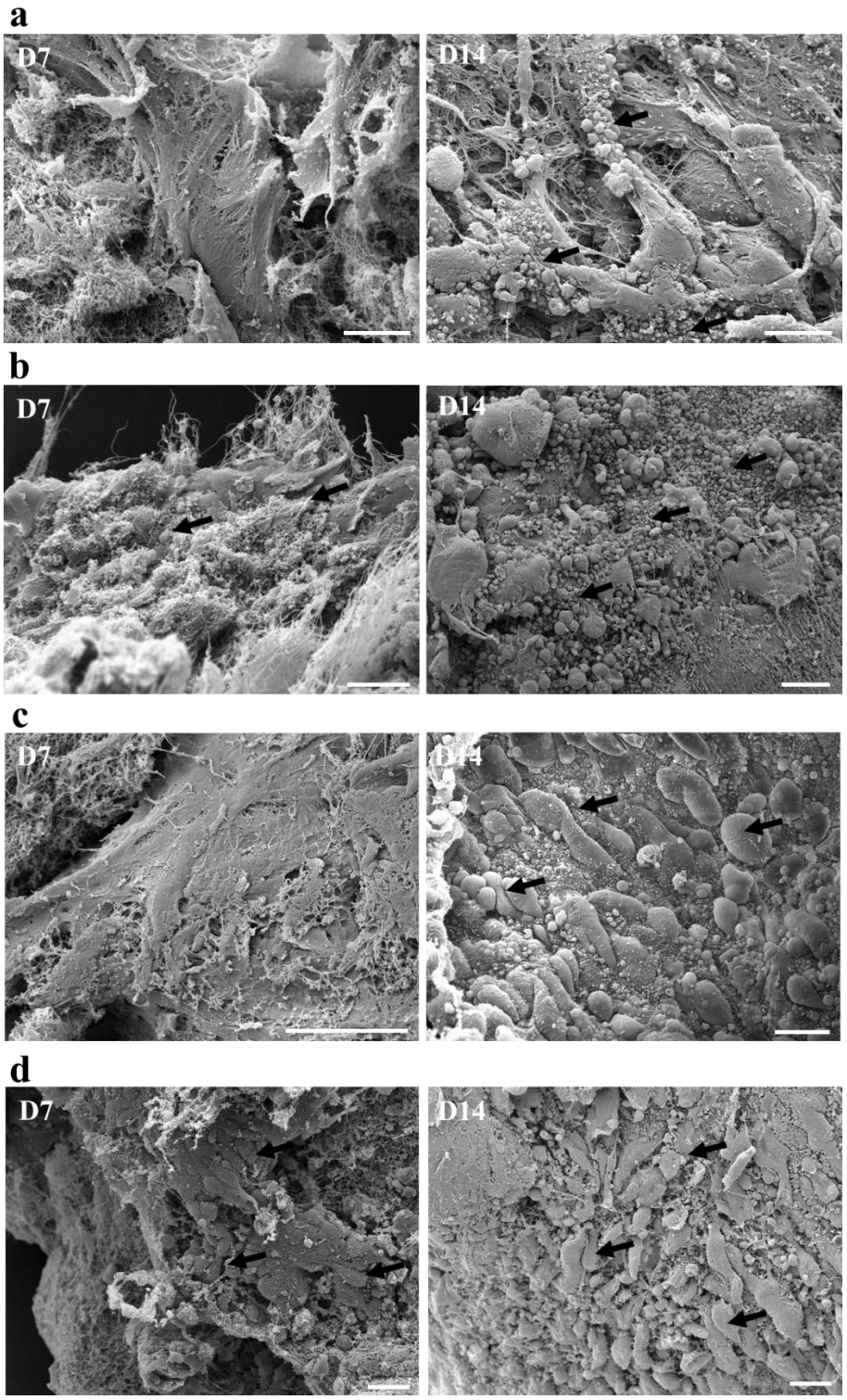

Figure 6. Calcium deposition and cell morphology after incubation during 7 and 14 days in osteogenic medium by scanning electron microscopy. (a) and (b) show the calcium deposition on low and high cell density hydrogels, respectively (black arrows). A faster and increased deposition is possible to be verified on $40x10^6$ cells/mL hydrogels. (c) and (d) demonstrate morphology changes during differentiation for low and high cell density samples, respectively. Cuboidal cells (black arrows) are already observable by day 7 on $40x10^6$ cells/mL hydrogels. The same only happens after 14 days of differentiation on low cell density specimens. Scale bars represent 10 µm ((a) and (b)) and 20 µm ((c) and (d)).

3.4. Osteogenic specific gene expression

Cells from the hydrogels were analysed for osteogenic specific genes using an RT-PCR array. At the lower cell density, it was observed that encapsulated cells showed higher expression of 48 genes (24 genes for skeletal development and 7 for bone mineral metabolism), with lower expression of 24 genes (11 genes correspond to skeletal development and 2 for bone mineral metabolism) at day 14, when compared to day 0 (figure 7(a)). Several markers of osteogenic differentiation had increased expression, including RUNX2 (more than 2-fold), SP7 (1.5-fold exchange), and BMP-2 (7.22-fold) (figure 7(c)). Reduced expression was observed for ALP, BGLAP and SPP1.

Hydrogels at the higher cell density showed increased expression of 67 genes (36 genes for skeletal development and 11 for bone mineral metabolism) over the 14-day period, with reduced expression of 22 genes (9 genes for skeletal development and 2 for bone mineral metabolism; figure 7(b)). The increased expression of RUNX2 (over 10-fold), SPP1 (higher than 7-fold), BMP-2 (over 300-fold), and BMP-6 (250-fold) were particularly notable (figure 7(d)). ALP and BGLAP showed reduced expression over the time course.

Finally, comparing the high and low cell density hydrogels at day 14, the higher density gel showed markedly increased expression of osteogenic biomarkers when compared to the lower density gel: RUNX2 (over 2.5-fold increase), SPP1 (nearly 15-fold) and BMP-2 (45-fold), BMP-3 (2-fold), BMP-6 (nearly 60-fold) and BMP-7 (4-fold). Contrarily, SP7, ALP and BGLAP, showed lower expression when comparing the high to low density gels at day 14.

4. Discussion

The ReJI system is the first drop-on-demand bioprinting system that can deposit cell-laden hydrogels with a high cell density. Impingement mixing is not a new concept, it has long been exploited for mixing air flows [33], and in the reactive injection moulding process to mix molten polymers [34]. In printing applications impingement mixing of droplets was first proposed for colour inkjet mixing [35]. There are also examples of twin valve or jet systems being used for bioprinting: with two adjacent valves being used with an on-substrate reaction [36], or to deliver two types of cell onto a surface [37]. GESIM offer a twin piezo system (TwinTip) for creating arrays of gel droplets on their Nano-plotter, and Visser et al report on the jetting of droplets into a stream of crosslinking solution to create encapsulated spheroids [38]. The unique elements of the ReJI system are that it offers a drop on demand system based on micro-valves, and these elements allow the system to 3D print high cell density gels.

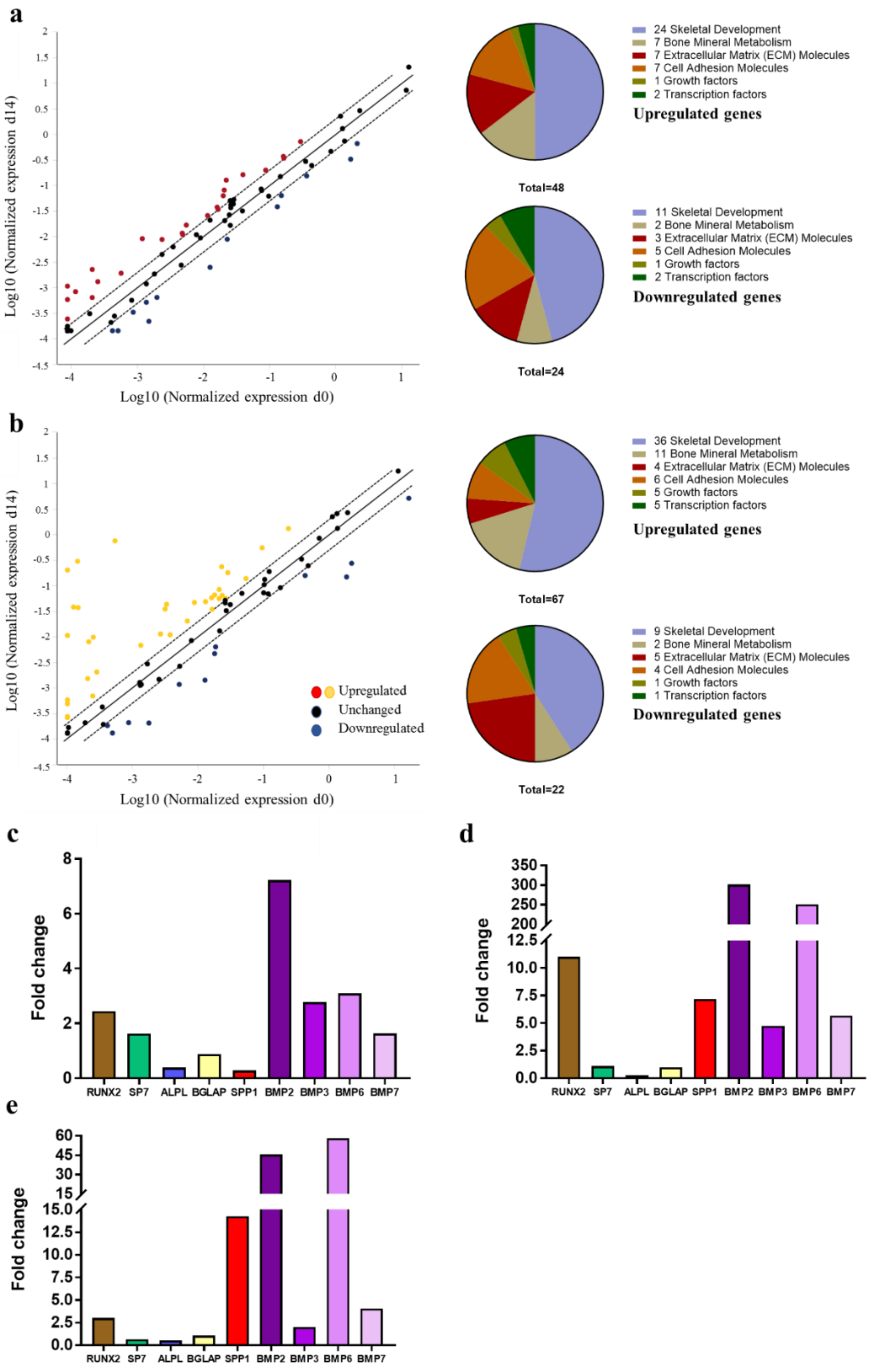

Figure 6. Osteogenic gene expression. (a) and (b) shows the gene expression comparison between 4M d14 to 4M d0, and 40M d14 to 40M d0. (c)-(e)exhibit the fold change of some of the most important osteogenic gene, comparing 4M d14 to 4M d0, 40M d14 to 40M d0, and 40M d14 to 4M d14, respectively. At day 14, $40x10^6$ cells/mL loaded gels present gene expression that reflects mature osteoblast formation, contrarily to $4x10^6$ cells/mL loaded gels that show pre-to-early osteoblast related gene expression.

The limitations of the ReJI process are that the system relies on rapid crosslinking to create gel droplets above the substrate, and that, as configured for this work, it is relatively low resolution, ~0.5-0.8 mm. The resolution of the system could be improved by using valves or jets with smaller orifices, but this would be expected reduce the upper limit in terms of achievable cell density. Table 1 compares our in-house technique to other common bioprinting techniques, to demonstrate that the system uniquely offers high cell density, with high cell viability, within a viscous gel, at high volume deposition rates.

Beyond jetting approaches, the Kenzan method [39], offers the most automated way of creating high cell density constructs, assembling pre-made cell spheroids to create tissue. Cell spheroid assembly delivers functional tissue without the need for a scaffold, but does require the generation of the spheroids prior to assembly. ReJI offers a process which delivers a lower cell density than cell spheroid assembly, but where the cell density is such that the cell-to-cell contact essential for tissue maturation is established in the printed gel. The use of ReJI for tissue development will require scaffolds, but it offers an alternative process for high cell density tissue pre-cursor development which does not require the generation of spheroids as a first step. The morphology shown in Figure 5 indicates that dense tissue-like structures are formed, along with spaces in the micro-tissue, which may arise from greater contractile forces in the high cell density gel, analogous to the contraction seen in spheroid development. Further work will be required to assess the relative productivity and efficiency of the alternative approaches to creating high cell density constructs.

Table 1 – Comparison between ReJI and other bioprinting techniques. Numbers are based on what is achievable for one deposition unit.

	ReJI bioprinting	Inkjet bioprinting	Single microvalve bioprinting	Extrusion bioprinting	Laser-assisted bioprinting	Ref.
Viscosity of Material Deposited on the Substrate	1–70 mPa/s	3–30 mPa/s	1–70 mPa/s	30 mPa/s to >$6x10^7$ mPa/s	1–300 mPa/s	19, 20, 40
Printing Speed	6 500 droplets/s	1 – 10 000 droplets/s	6 500 droplets/s	10 µm/s – 700 mm/s.	100 – 5000 droplets/s	19, 20, 41-47
Volume deposition rate	80 µL/s	160 µL/s	40 µL/s	3-15 µL/s	175 - 1800 nL/s	41, 47-50
Resolution	100-300 nL droplets	pL droplets	pL to nL droplets	5 µm to mm size deposited track	<pL droplets	19, 46
Cell viability	>90%	>85%	>90%	40-80%	>95%	19, 46
Crosslinking Process	In process	Post-printing	Post-printing	Pre-, post-printing	Post-printing	19, 42
Cell density	$9x10^7$ cells/mL	Low, <$5x10^6$ cells/mL	High, 10^7/mL	High, cell spheroids	High, 10^8 cells/mL	19, 20, 46

To obtain the developed microtissues, 14 days of incubation in osteogenic medium at 37°C and 5% CO_2 was necessary. The 30% hydrogel mass loss may be connected to poorly crosslinked branches inside the CAF gel structure being washed off during the incubation period. The 3 mm thick CAF hydrogel was able to quickly absorb dissolved molecules with saturation in less than 1 hour. This guarantees stability of cells during their development. The interconnected porous network in the gel is essential for building up microtissues based on high cell densities, as cell migration will be necessary for tissue development [51-53]. This porous network is preserved over a 14-day period, making this hydrogel ideal for tissue development applications.

Cells survive the jetting and impingement processes. This is explained by the low viscosity of both cell carrier ink (crosslinking solution) and gel precursor. When leaving the microvalve nozzle, cells suffer little shear stress due to the low viscosity of the crosslinker solution. Additionally, when mixing, the fast reaction instantly encapsulates the cells, giving them protection when droplet reaches the substrate, but also assuring elasticity (that fibrin enriched hydrogels are recognized for [54,55]) to minimize stress on impact. The impingement and quick reaction are a pre-requisite for forming well defined multi-layer structures. The modulus obtained for the acellular bioprinted gel (1.1 kPa) is very similar to the modulus of similar gel formulations when prepared conventionally (0.9-1.3kPa) [30]. One and two weeks after printing, cell viability is maintained, as fibrin and collagen are biocompatible natural materials that are widely used as scaffold materials due to their properties, including extracellular matrix promotion [56,57]. Precise structures were printed using two different cell density inks, producing hydrogels with an average of $6x10^5$ and $5x10^6$ cells for the low and high cell density hydrogels, respectively.

Cell detachment is considered as the main reason for cell number decrease on high cell density hydrogels on day 7. The cell numbers reported in Figure 4 are the numbers of cells in the gel. In the high cell population gels some cells migrate out of the gel into the surrounding media, which means that we have three main cellular mechanisms operating in parallel. For the high cell density gel migration and differentiation seem to dominate in week 1, while in week 2 proliferation and differentiation dominate. This cell migration out of the gel is not necessarily a bad thing, as the benefit of having a highly confluent gel is clearly seen in Figs 5-7. Contrarily, for the low cell density hydrogels, proliferation seems to be the dominant mechanism in week 1, with differentiation in week 2. Microtissue development is dependent on several factors, including cell density, mechanical forces and the presence of extracellular matrix [58-62]. Here, we reinforce past studies, with special focus on the importance of high cell densities in 3D structures to obtain fast and developed microtissues by direct differentiation [15, 57, 63].

Increased calcium deposition on the higher cell density hydrogels is assumed to be a result of a faster rate of MSC differentiation into osteoblasts. This was confirmed by the presence of cuboidal cells, a morphology which is associated with mature osteoblasts [64], already by day 7. ALP, an early osteogenic marker, supports this view. Increased ALP concentrations were produced at day 0, when compared to day 7 and 14, with the higher

cell density hydrogels presenting the lowest concentration at day 14, as ALP levels are downregulated by the end of the osteogenesis [65, 66].

Gene expression was also influenced by cell density. Typical pre-osteoblastic behaviour was observed on low cell density hydrogels due to the increased expression of RUNX2 and SP7 and reduced expression of BGLAP and SPP1 [67]. BMPs, intrinsically connected to bone formation, also increased expression.

This work has shown that cell density is crucial to the rate of functional bone microtissue formation. In cancer and in other diseases there is a clear commercial need for improved models for large scale screening, and microtissue models are considered to offer significant potential [68,69]. To date the scalability and reliability of microtissue models has been identified as limitations, with these issues closely related [14,70]. A lack of scalability means that limited replicates of any given experiment can be made, and a lack of replicates makes it difficult to understand variation in statistical terms. By reliably depositing cells and materials at rates which allow for thousands of micro-tissue precursors to be generated per hour the ReJI technology has potential to address a key problem in terms of micro-tissue model development and exploitation. Future work will address understanding the limits in terms of resolution, integrating the technique with scaffold manufacturing processes to create composite tissue engineered structures, and use of the technique to create co-cultures at high throughput rates.

5. Conclusion

This study describes the development and characterisation of high cell density cell-laden hydrogels produced via reactive jet impingement. The fabricated CAF hydrogels presented high uptake capability, which is essential for cell maintenance, and porous structures, that were conserved after 14-days of incubation. The hydrogels supported cell viability, proliferation, migration and promoted osteogenic differentiation of bMSCs. The ReJI system was able to printing bio-inks with a cell density of $40x10^6$ cells/mL. Cell density was revealed to be key for microtissue formation through assessment of osteogenic specific markers, as well as to the increased deposition of calcium. In addition, cell differentiation was demonstrated to be faster at higher cell densities cell-laden hydrogels. The ReJI process offers a new and valuable approach to bioprinting with high cell density gels.

Acknowledgements

The work reported in this article was funded by the EPSRC Centre for Innovative Manufacture in Medical Devices (EP/K029592/1), the Arthritis Research UK Tissue Engineering Centre (Award 21156) and the Newcastle University MRC Confidence in Concept Fund. R.D.C.R. acknowledges support from Newcastle University for his Ph.D. studentship. DP was funded by an NC3Rs Training Fellowship and CCLG, Little Princess Trust project grant. The authors also thank T. Booth and the Bioimaging Unit

(Newcastle University, U.K.) and the Electron Microscopy Research Services (Newcastle University, U.K.) for image acquisition and Ryan Nelson for the support given on the gene expression experiments. Data supporting this publication is openly available under an 'Open Data Commons Open Database License'. Additional metadata are available at: http://dx.doi.org/10.17634/122951-6.

References

[1] Pampaloni F, Reynaud E, Stelze E 2007 The third dimension bridges the gap between cell culture and live tissue *Nat. Rev. Mol. Cell Biol.* **8**, 839-845

[2] Russel S, Wojtkowiak J, Neilson A, Gillies, R 2017 Metabolic Profiling of healthy and cancerous tissues in 2D and 3D *Sci. Rep.* **7**, 15295

[3] Edmondson R, Broglie J, Adcock A, Yang L 2014 Three-Dimensional Cell Culture Systems and Their Applications in Drug Discovery and Cell-Based Biosensors *Assay Drug Dev Technol.* **12**, 207-218

[4] Stock K, Estrada M., Vidic S, Gjerde K, Rudisch A, Santo V, Barbier M, Blom S, Arundkar S, Selvam I, Osswald A, Stein Y, Gruenewald S, Brito C, Weerden W, Rotter V, Boghaert E, Oren M, Sommergruber W, Chong Y, de Hoogt R, Graeser R. 2016 Capturing tumor complexity in vitro: Comparative analysis of 2D and 3D tumor models for drug discovery *Sci. Rep.* **6**, 28951

[5] Huh D, Hamilton G, Ingber D 2011 From 3D cell culture to organs-on-chips *Trends Cell Biol.* **21**, 745-754

[6] de Souza N 2018 Organoids *Nat. Methods* **15**, 23

[7] Mosaad E, Chambers K, Futrega K, Clements J A, Doran M R 2018 The Microwell-mesh: A high-throughput 3D prostate cancer spheroid and drug-testing platform *Sci. Rep.* **8**, 253

[8] Thakuri P, Liu C, Luker G, Tavana H 2018 Biomaterials-Based Approaches to Tumor Spheroid and Organoid Modeling *Adv. Healthc. Mater.* **7**, 1700980

[9] Di Maggio N, Piccinini E, Jaworski M, Trumpp A, Wendt D J, Martin I 2011 Toward modeling the bone marrow niche using scaffold-based 3D culture systems *Biomaterials* **32**, 321-329

[10] Thoma C, Zimmermann M, Agarkova I, Kelm J M, Krek W 2014 3D cell culture systems modeling tumor growth determinants in cancer target discovery *Adv. Drug Deliv. Rev.* **69-70**, 29-41

[11] Breslin S, O'Driscoll L 2013 Three-dimensional cell culture: the missing link in drug discovery *Drug Discov. Today* **18**, 240-249

[12] Friedrich J, Eder W, Castaneda J, Doss M, Huber E, Ebner R, Kunz-Schughart L A 2007 A Reliable Tool to Determine Cell Viability in Complex 3-D Culture: The Acid Phosphatase Assay *J. Biomol. Screen* **12**, 925-937

[13] Van Duinan V, Trietsch S, Joore J, Vulto P, Hankemeir T 2015 Microfluidic 3D cell culture: from tools to tissue models *Curr. Opin. Biotechnol.* **35**, 118-126

[14] Junaida A, Mashaghia A, Hankemeiera T, Vulto P 2017 An end-user perspective on Organ-on-a-Chip: Assays and usability aspects *Curr. Opin. Biomed. Eng*, **1**, 15-22

[15] Faulkner-Jones A, Fyfe C, Cornelissen D, Gardner J, King J, Courtney A, Shu W 2016 Bioprinting of human pluripotent stem cells and their directed differentiation into hepatocyte-like cells for the generation of mini-livers in 3D *Biofabrication* **7**

[16] Ma X, Qu X, Zhu W, Li Y-S, Yuan S, Zhang H, Liu J, Wang P, Lai C S E, Zanella F, Feng G-S, Sheikh F, Chien S, Chen S 2016 Deterministically patterned biomimetic human iPSCderived hepatic model via rapid 3D bioprinting *Proc. Natl. Acad. Sci. U.S.A* **113**, 2206-2211

[17] Zhang K, Fu Q, Yoo J, Chen X, Chandra P, Mo X, Song L, Atala A, Zhao W 2017 3D bioprinting of urethra with PCL/PLCL blend and dual autologous cells in fibrin hydrogel: An in vitro evaluation of biomimetic mechanical property and cell growth environment *Acta Biomater.* **50**, 154-164

[18] Kang H W, Lee S J, Ko I K, Kengla C, Yoo J J, Atala A 2016 A 3D bioprinting system to produce human-scale tissue constructs with structural integrity *Nat. Biotechnol.* **34**, 312-319

[19] Murphy S V, Atala, A 2014 3D bioprinting of tissues and organs *Nat. Biotechnol.* **32**, 773-785

[20] Donderwinkel I, Van Hest J C M, Cameron N R 2017 Bio-inks for 3D bioprinting: recent advances and future prospects *Polym. Chem.* **8**, 4451-4171

[21] Ozbolat I T, Hospdiuk M 2016 Current advances and future perspectives in extrusion-based bioprinting *Biomaterials* **76**, 321-343

[22] Norotte C, Marga F S, Niklason L E, Forgacs G 2009 Scaffold-free vascular tissue engineering using bioprinting *Biomaterials* **30**, 5910-5917

[23] Ong C S, Fukunishi T, Zhang H, Huang C Y, Nashed A, Blazeski A, DiSilvestre D, Vricella L, Conte J, Tung L, Tomaselli G F, Hibino N 2017 Biomaterial-Free Three-Dimensional Bioprinting of Cardiac Tissue using Human Induced Pluripotent Stem Cell Derived Cardiomyocytes *Sci. Rep.* **7**, 4566

[24] Marga F, Jakab K, Khatiwala C, Shepherd B, Dorfman S, Hubbard B, Colbert S, Gabor F 2012 Toward engineering functional organ modules by additive manufacturing *Biofabrication* **4**

[25] Katt M, Placone A L, Wong A D, Xu Z S, Searson P C 2016 In Vitro Tumor Models: Advantages, Disadvantages, Variables, and Selecting the Right Platform *Front. Bioeng. Biotechnol.* **4**

[26] Castillo L R C, Oancea A, Stüllein C, Régnier-Vigouroux A 2016 Evaluation of Consistency in Spheroid Invasion Assays *Sci. Rep.* **6**, 28375

[27] Ávila H M, Schwarz S, Rotter N, Gatenholm P 2016 3D bioprinting of human chondrocyte-laden nanocellulose hydrogels for patient-specific auricular cartilage regeneration *Bioprinting* **1-2**, 22-35

[28] Levato R, Visser J, Planell J A, Engel E, Malda J, Mateos-Timoneda M A 2014 Biofabrication of tissue constructs by 3D bioprinting of cell-laden microcarriers *Biofabrication* **6**

[29] James S, Fox J, Afsari F, Lee J, Clough S, Knight C, Ashmore J, Ashton P, Preham O, Hoogduijn M, Ponzoni Rde A, Hancock Y, Coles M, Genever P 2015 Multiparameter Analysis of Human Bone Marrow Stromal Cells Identifies Distinct Immunomodulatory and Differentiation-Competent Subtypes *Stem Cell Reports* **4**, 1004-1015

[30] Montalbano G, Toumpaniari S, Popov A, Duan P, Chen J, Dalgarno K, Scott III W E, Ferreira A M 2018 Synthesis of bioinspired collagen/alginate/fibrin based hydrogels for soft tissue engineering *Mater. Sci. Eng. C.* **91**, 236-246

[31] Patent GB1710834.1, "Printing apparatus and method", 2017.

[32] Donovan F M, Cunningham D D 1998 Signaling Pathways Involved in Thrombin-induced Cell Protection *J. Biol. Chem.* **273**, 12746-12752

[33] Webb B W, Ma C-F 1995 Single-Phase Liquid Jet Impingement Heat Transfer *Advances in Heat Transfer*, **26**, 105-217

[34] Lee L J, Ottino, J M, Ranz, W E, Macosko C W 1980 Impingement mixing in reaction injection molding *Polymer Engineering and Science* **20** 868-874.

[35] Patent Application DE3501905A1, "Method of colour recording of information by means of ink jet", 1985.

[36] Li C, Faulkner-Jones A, Dun A R, Jin J, Chen P, Xing Y, Yang Z, Li Z, Shu W, Liu D, Duncan R R 2015 Rapid formation of a supramolecular polypeptide-DNA hydrogel for in situ three-dimensional multilayer bioprinting *Angewandte Chemie* **53** 4029-4033.

[37] Xu F, Celli J, Rizvi, I, Moon S, Hasan T, Demirci U 2011 A three‐dimensional in vitro ovarian cancer coculture model using a high‐throughput cell patterning platform *Biotechnology Journal* **6** 204-212.

[38] Visser C W, Kamperman T, Karbaat, L P, Lohse D, Karperien, M 2018 In-air microfluidics enables rapid fabrication of emulsions, suspensions, and 3D modular (bio)materials Science Advances, **4**, doi: 10.1126/sciadv.aao1175

[39] Moldovan N I, Hibino N, and Nakayama K 2017 Principles of the Kenzan Method for Robotic Cell Spheroid-Based Three-Dimensional Bioprinting *Tissue Engineering Part B: Reviews* **23**, doi: 10.1089/ten.teb.2016.0322

[40] Ng, W L, Lee J M, Yeong W Y, Naing M W 2017 Microvalve-based bioprinting – process, bio-inks and applications *Biomater. Sci.* **5**, 632-647

[41] Gudapati H, Dey M, Ozbolat I 2016 A comprehensive review on droplet-based bioprinting: Past, present and future *Biomaterials* **102**, 20-42

[42] Lee J M, Yeong W Y 2016 Design and Printing Strategies in 3D Bioprinting of Cell‐Hydrogels: A Review *Adv. Healthc. Mater.* **5**, 2856-2865

[43] Bakshinejad A, D'Souza R M 2015 A Brief Comparison Between Available Bio-printing Methods *Proc. IEEE Great Lakes Biomedical Conference (GLBC)*

[44] Hölzl K, Lin S, Tytgat L, Van Vlierberghe S, Gu L, Ovsianikov A 2016 Bio-ink properties before, during and after 3D bioprinting *Biofabrication* **8**, 032002

[45] Gao G, Huang Y, Schilling A F, Hubbell K, Cui X 2018 Organ Bioprinting: Are We There Yet? *Adv. Healthc. Mater.* **8**, 1701018

[46] Ozbolat I T 2017 3D Bioprinting: Fundamentals, Principles and Applications, Chapter 5. Elsevier

[47] Guillotin B, Souquet A, Catros S, Duocastella M, Pippenger B, Bellance S, Bareille R, Rémy M, Bordenave L, Amédée J, Guillemot F 2010 Laser assisted bioprinting of engineered tissue with high cell density and microscale organization *Biomaterials* **31**, 7250-7256

[48] Graham A D, Olof S N, Burke M J, Armstrong J P K, Mikhailova E A, Nicholson J G, Box S J, Szele F G, Perriman A W, Bayley H 2017 High-Resolution Patterned Cellular Constructs by Droplet-Based 3D Printing *Sci. Rep.* **7**, 7004

[49] Liu W, Zhong Z, Hu N, Zhou Y, Maggio L, Miri A K, Fragasso A, Jin X, Khademhosseini A, Zhang Y S 2018 Coaxial extrusion bioprinting of 3D microfibrous constructs with cell-favorable gelatin methacryloyl microenvironments *Biofabrication* **10**, 024102

[50] Koch L, Brandt O, Deiwick A, Chichkov B 2017 Laser-assisted bioprinting at different wavelengths and pulse durations with a metal dynamic release layer: A parametric study *Int. j. bioprinting* **3**, 42-53

[51] Campell J, Husmann A, Hume R D, Watson C J, Cameron R E 2017 Development of three-dimensional collagen scaffolds with controlled architecture for cell migration studies using breast cancer cell lines *Biomaterials* **114**, 34-43

[52] Yamada K M, Cukierman E 2007 Modeling Tissue Morphogenesis and Cancer in 3D *Cell* **130**, 601-610

[53] Ma L, Zhou C, Lin B, Li W 2010 A porous 3D cell culture micro device for cell migration study *Biomed. Microdevices* **12**, 753-760

[54] Janmey P A, Winer J P, Weisel J W 2009 Fibrin gels and their clinical and bioengineering applications *J. Royal Soc. Interface* **6**, 1-10

[55] Piechocka I K, Babacac R G, Potters M, Mackintosh F C, Koenderink G H 2010 Structural Hierarchy Governs Fibrin Gel Mechanics *Biophys. J.* **98**, 2281-2289

[56] Hong H, Stegemann J P 2008 2D and 3D collagen and fibrin biopolymers promote specific ECM and integrin gene expression by vascular smooth muscle cells *J. Biomater. Sci. Polym. Ed.* **19**, 1279-1293

[57] Chan E C, Kuo S M, Kong A M, Morrison WA, Dusting G J, Mitchell G M, Lim S Y, Liu G S 2016 Three-Dimensional Collagen Scaffold Promotes Intrinsic Vascularisation for Tissue Engineering Applications *PLoS One* **22**, e0149799

[58] Nelson C M, Chen C S 2002 Cell-cell signaling by direct contact increases cell proliferation via a PI3K-dependent signal *FEBS Lett.* **514**, 238-242

[59] Liu A, Wang H, Copeland C, Chen C S, Shenoy V B, Reich D H 2016 Matrix viscoplasticity and its shielding by active mechanics in microtissue models: experiments and mathematical modelling *Sci. Rep.* **6**, 33919

[60] Griffith L G, Swartz M A 2006 Capturing complex 3D tissue physiology in vitro *Nat. Rev. Mol. Cell Biol.* **7**, 211-224

[61] Legant W R, Pathak A, Yang M, Deshpande V S, McMeeking R M, Chen C S 2009 Microfabricated tissue gauges to measure and manipulate forces from 3D microtissues *Proc. Natl. Acad. Sci. U.S.A* **106**, 10097-10102

[62] Ladoux B, Mège R 2017 Mechanobiology of collective cell behaviours *Nat. Rev. Mol. Cell Biol.* **18**, 743-757

[63] Bishop, E S, Mostafa S, Pakvasa M, Luu H H, Lee M J, Wolf J M, Ameer G A, He T C, Reid R R 2017 3-D bioprinting technologies in tissue engineering and regenerative medicine: Current and future trends *Genes & Diseases* **4**, 185-195

[64] Hwang N S, Varghese S, Elisseeff J 2008 Controlled differentiation of stem cells *Adv. Drug Deliv. Rev.* **60**, 199-214

[65] Liu F, Malaval L, Aubin J E 1997 The Mature Osteoblast Phenotype Is Characterized by Extensive Plasticity *Exp. Cell Res.* **232**, 97-105

[66] Golub E E, Boesze-Battaglia K 2007 The role of alkaline phosphatase in mineralization *Curr. Opin. Orthop.* **18**, 444-448

[67] Wagner E R, He B C, Chen L, Zuo G W, Zhang W, Shi Q, Luo Q, Luo X, Liu B, Luo J, Rastegar F, He C J, Hu Y, Boody B, Luu H H, He T C, Deng Z L, Haydon R C 2010 Therapeutic Implications of PPARgamma in Human Osteosarcoma *PPAR Res.* **2010**, 956427

[68] Aubin J E 2008 Mesenchymal Stem Cells and Osteoblast Differentiation. In *Principles of Bone Biology*, 85-107 Cambridge, Massachusetts: Academic Press.

[69] Rodriguez-Dévora J, Zhang B, Reyna D, Shi Z D, Xu T High throughput miniature drug-screening platform using bioprinting technology *Biofabrication* **4**, 035001.

[70] Peng W, Datta P, Ayan B, Ozbolat V, Sosnoski D, Ozbolat I T 2017 3D bioprinting for drug discovery and development in pharmaceutics *Acta Biomater.* **57**, 26-46